Dynamic Analysis of a High-Bandwidth, Large-Strain, PZT Cellular Muscle Actuator with Layered Strain Amplification

Thomas W. Secord, Jun Ueda, and H. Harry Asada

***Abstract*— This paper presents the dynamic analysis of an artificial muscle actuator designed for high-bandwidth, power-law strain amplification. The actuator is based on a nested cellular architecture of PZT stack actuators. Most smart material actuators have seen limited use in mobile robotic applications because of their small strain, low stress capacity, low bandwidth, and stringent input requirements. The proposed actuator design overcomes these limitations and can serve as a high-bandwidth multifunctional artificial muscle. The dynamic characteristics of the actuator design are derived analytically and validated experimentally. A test system mimicking flapping flight is then used to illustrate the multifunctional actuator dynamics. Design guidelines are discussed for both resonance and servo applications.**

I. INTRODUCTION

In addition to generating force and displacement, muscles can store and dissipate energy due to their viscoelastic nature. Animals exploit the multi-functional muscle characteristics for energy efficient running, flying, and swimming as well as for adaptive negotiation of varying environments [1]. Traditional DC and AC motors do not have compliance in their inherent physical construction. Rather, external springs and compliant elements must be attached to the electric motors in order to store strain energy and exhibit flexible behavior.

The robotic community has been studying a combination of rigid actuators and springs for nearly four decades. For manipulation, elastic fingers with built-in springs were constructed in the 70s [2]; Raiberts hopping robots [3] exploited coil springs incorporated into hydraulic cylinders for stable and energy-efficient dynamic locomotion [4]; Cutkoskys cockroach robots were equipped with tuned viscoelastic legs made from a layered manufacturing process [5]. For flying with flapping wings, compliance characteristics at the wing structure or at external springs attached to the system play an important role [6], [7]. In particular, resonance between the wings and the actuators allows for energy efficient flying [7], [23]. A number of effective design concepts have recently been developed in biologically inspired robots [8], [9], [10], [11].

If an actuator possesses tunable compliance inherent in its structure, robots may be more efficient and dexterous. One of the aims of artificial muscle research is to develop actuators with inherent compliance. These actuators must be seamlessly integrated into the overall structural design in order to meet the demands for energy efficiency and dexterity. Pneumatic actuators, in particular rubberators, exhibit substantial compliance. These actuators are useful for building flexible arms, hands, and exoskeletons that are safe for human interaction [12], [13]. Polypyrrole and other conducting polymer actuators also exhibit viscoelastic properties inherently [14], [15]. Dielectric elastomers that entail pre-loading structures are inherently compliant [16], while shape memory alloys can vary compliance and damping characteristics with phase changes [17].

For high speed locomotive robots and maneuverable flapping robots, actuator bandwidth is an important specification. Compliance must be tunable so that the control system has a broad bandwidth, yet it can resonate with the load at a desired frequency for maximizing efficiency. Existing muscle actuator materials, although promising for many other applications, do not meet the high bandwidth or high efficiency requirements for mimicking biological systems. Piezoelectric actuators such as lead zirconate titanate (PZT) have extremely high bandwidth and high efficiency, which makes them appropriate for mobile robot applications [6]. The most critical drawback of PZT, however, is its extremely small strain of only 0.1 %. This has limited its application to only micro robots and other small load applications. However, recently an effective mechanism for amplifying strain has been found [18].

With use of a layered strain amplification mechanism the effective strain of PZT stack actuators can be exponentially increased, achieving over 20% displacement compared to its body length. This large strain would allow the actuators to be used in the same manner as natural skeletal muscles, which produce approximately 20% strain. Furthermore, the PZT stack actuator has a high bandwidth, large stress capacity, and stable material properties. Combined with the compliant layered strain amplification mechanisms, the high strain actuator has the potential to be used in high speed, high efficiency mobile robots. The objective of this paper is to analyze the dynamics of the high strain PZT actuator and to explore the possibility of building actuators that can resonate with the load as well as achieve high bandwidth control.

II. LAYERED STRAIN AMPLIFICATION DESIGN

Fig. 1 shows the design concept of a hierarchical strain amplification mechanism [18]. The displacement created by PZT stack actuators is increased exponentially with multiple layers of amplification mechanism. The basic unit creating a

T. Secord, J. Ueda, and H. H. Asada are with the Department of Mechanical Engineering, Massachusetts Institute of Technology, Cambridge, MA, USA {secord,uedajun,asada}@mit.edu .

J. Ueda is also with the Graduate School of Information Science, Nara Institute of Science and Technology, Ikoma, Nara, Japan.

Preprint submitted to 2008 IEEE International Conference on Robotics and Automation. Received September 14, 2007.

displacement is a PZT stack actuator packed in a rhombus-shaped strain amplifier. As shown on the top left corner of Fig. 1, the displacement of the PZT stack actuator in the horizontal direction is amplified with this mechanism, resulting in a larger displacement in the vertical direction. This type of amplification is a standard technique in the literature.

The unique aspect of the layered design is that several of these PZT units are connected together and then enclosed with a larger rhombus strain amplification mechanism. Furthermore, several of these larger units are then connected together and are placed in an even larger rhombus amplifier. As this process is repeated, the effective strain increases exponentially. Fig. 1 includes three different sizes of the rhombus mechanism, creating a three-layer strain amplifier.

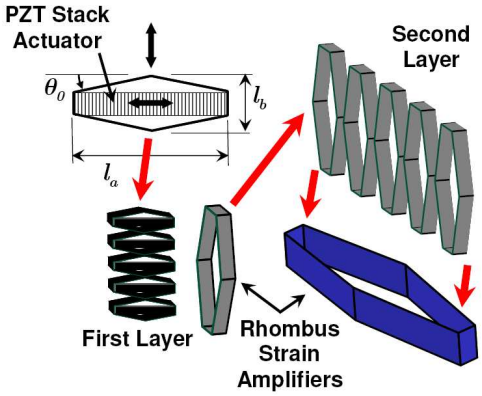

Fig. 1. Layered architecture of strain amplification devices

The effective strain is the ratio of output displacement to the original body length in the same output direction. Due to the aspect ratio of the rhombus mechanism, l_a/l_b, shown in Fig. 1, the effective strain amplification is the product of the displacement amplification gain and this aspect ratio. Let θ_0 be the angle of an oblique edge of the rhombus at a nominal state as shown in Fig. 1. The displacement amplification gain is given by $\cot\theta_0$ and the resultant gain of effective strain amplification g is therefore given by

$$g = \frac{l_a}{l_b}\cot\theta_0. \tag{1}$$

If each layer has the same value of g and the number of layers is K, the effective strain amplification of the assembly is g^K. Considering practical design requirements, a typical value of displacement amplification is $\cot\theta_0 = 5$, while the aspect ratio is typically near 3. If two layers of amplification are used, the effective gain becomes $(5 \times 3)^2 = 225$. Although the strain of PZT is extremely small, around 0.1 %, the resultant effective strain of the layered system is over 20%.

Fig. 2 illustrates a possible biological robot application of this large strain PZT actuator. The artificial muscle shown in the figure consists of five stacks of second-layer units. As shown, the cellular architecture allows the PZT actuator to be

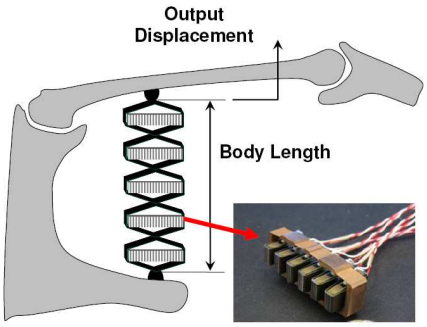

Fig. 2. Application of a cellular PZT actuator to a skeletal structure

used in a way similar to the anatomical structure of animal muscles. Fig. 2 also shows a picture of prototype actuator: one unit of the second-layer PZT actuator, consisting of six first-layer units and an outer rhombus. The prototype is discussed in more detail in subsequent sections.

This layered strain amplification design has the potential to be a promising muscle actuator. The dynamic behavior of the system, however, may be complex due to the multi-layer structure, which posesses several design parameters. The following sections address the dynamic modeling and experimental verification of the proposed system, followed by an application to flapping actuation.

III. MULTILAYER ACTUATOR DYNAMICS

The dynamics of a fully assembled actuator as shown in Fig. 2 are very complex due to the abundance of closed kinematic chains and unit interconnections. The scope of this work is to address the most fundamental subsystem dynamics and their implications for mobile robot design. This section provides the dynamic analysis of a serial connection of N_2 second layer units as shown in Fig. 3, followed by the analysis of a single unit as a limiting case. Throughout the analysis, the first layer units are treated abstractly as lumped elements suspended within the second layer structure. This choice is justified since experimental data indicate that the dynamics of the first layer units are unimodal with a natural frequency well outside the bandwidth of the second layer.

A. Modeling Assumptions

When a rhombus structure is modeled as a closed loop kinematic chain with revolute joints and a single grounded link, Gruebler's equation indicates that the mechanism has 5 degrees of freedom. Moreover, several geometric inversions exist within the mechanism that increase the modeling complexity.

The primary assumption in the dynamic model will be that the flexural joints of the rhombus act as revolute joints with overlaid torisonal springs. These springs are denoted by k_a and k_c for the rhombus apexes and corners respectively. The torsional stiffness of the flexures can be obtained from the standard linear beam theory:

Preprint submitted to 2008 IEEE International Conference on Robotics and Automation. Received September 14, 2007.

$$k_{a,c} = \frac{Ebt_f^3}{12L_f}, \tag{2}$$

where E is the elastic modulus of the rhombus material, t_f is the flexure thickness of the apex or corner, and L_f is the thickness of the flexure leaf at the apex or corner. To further simplify the analysis, the following additional assumptions are used:

- The serial chain of units is constrained to move along a single axis
- The units in the serial chain are rigidly connected
- The base rhombus mechanism is grounded to an inertial frame $O-XY$
- The motion of the rhombus links is symmetric about the vertical and horizontal centerlines.
- The units are identically sized with identical equilibrium configurations quantified by θ_0
- The thick sections of the rhombus are perfectly rigid
- The oblique rhombus beams have mass and rotational inertia
- The inner first layer units will act as a suspended mass as shown in Fig 4 (b).

The serial system is shown in Fig. 3. With the units constrained to move along the Y-axis, there is no lateral sway mode introduced. The assumption of rhombus symmetry about the centerlines allows each rhombus to be modeled with two generalized coordinates ϕ_i and y_{pi} as shown in Fig 3. The angle ϕ_i denotes the excursion of the ith unit's oblique links away from the equilibirium angle θ_0, and y_{pi} denotes the position of the ith unit's suspended mass with respect to the local horizontal centerline. A single unit is shown in detail in Fig. 4 (a). The lumped compliance elements are shown in Fig 4 (b). Notice that the first layer force is introduced using a pure force source f_0 acting in parallel with the compliance k_x. Therefore, the k_x parameter represents a combination of the moonie mechanism stiffness along its output as well as the equivalent parallel combination of the PZT stiffness and the moonie input stiffness.

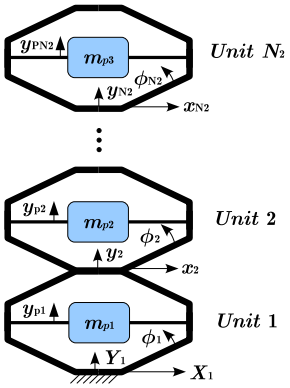

Fig. 3. Dynamic model for a serial connection of a second layer units

The PZT acts a pure force source in parallel with a stiffness k_{pzt}. Assuming linear behavior, the PZT actuator output

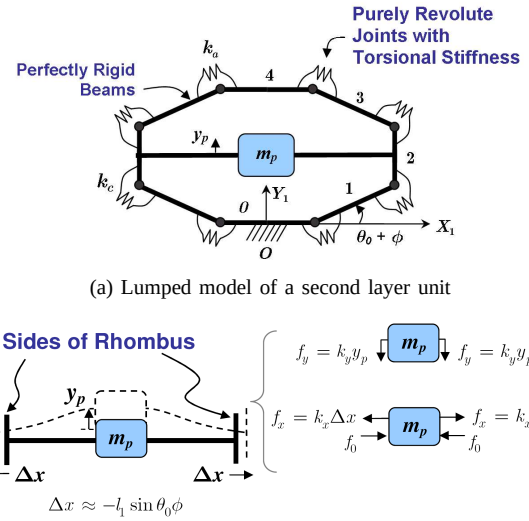

(a) Lumped model of a second layer unit

(b) Detailed view of suspended lumped mass and compliance elements

Fig. 4. Dynamic lumped parameter model of a second layer unit

strain is related to the applied electrical field through the piezoelectric coefficient d_{33}. Strictly speaking, the piezoelecric stiffness and strain coefficent are not constants. However, for simplicity, the following analysis assumes constant PZT parameters. Thus, if the force output of the stack is denoted by f_{pzt}, the output stack displacememt is Δx_{pzt}, and the number of films in the stack is N_{film}, then

$$f_{pzt} = k_{pzt}(\beta V - \Delta x_{pzt}), \tag{3}$$

where $\beta = N_{film} d_{33}$ and V is the applied voltage. From (3), note that the force is a maximum when the displacement is set to be zero. This is called the blocking force f_{pzt}^{block} and it corresponds to placing the stack between perfectly rigid supports. Assuming the maximum allowable voltage is applied, then the blocked force is given by $k_{pzt}\beta V_{max}$. Similarly, the displacement under free end conditions is referred to as the the free displacement Δx_{pzt}^{free} and is given by βV_{max}.

B. Dynamics of Serially Connected Second Layer Units

In the absence of lateral sway, the kinematics of a second layer chain can be determined in terms of the link unit vectors $\hat{\mathbf{e}}_{ij}$. The first subscript $i = 1, 2, ..., N_2$ indicates the unit number as shown in Fig. 3 and the second subscript $j = 0, 1, ..., 4$ indicates the link number as shown in Fig. 4 (a). The general link unit vectors can be written more explicitly as follows:

$$\hat{\mathbf{e}}_{ij} = \begin{cases} \hat{\mathbf{i}} & j = 0 \\ \cos(\theta_0 + \phi_i)\hat{\mathbf{i}} + \sin(\theta_0 + \phi_i)\hat{\mathbf{j}} & j = 1 \\ \hat{\mathbf{j}} & j = 2 \\ -\cos(\theta_0 + \phi_i)\hat{\mathbf{i}} + \sin(\theta_0 + \phi_i)\hat{\mathbf{j}} & j = 3 \\ -\hat{\mathbf{i}} & j = 4 \end{cases}$$

Preprint submitted to 2008 IEEE International Conference on Robotics and Automation. Received September 14, 2007.

Denoting the length of the jth link as l_j, the velocity of the center of mass of the jth link of unit i $(i \geq 2, j \geq 1)$ with respect to the base inertial frame is then given by

$$\begin{aligned}\mathbf{v}_{Cij} &= \sum_{s=1}^{i-1} 2l_1\dot{\phi}_s \cos(\theta_0+\phi_s)\hat{\mathbf{j}} \\ &\quad + \sum_{r=1}^{j} \tfrac{1}{2}(l_{r-1}\tfrac{d\hat{\mathbf{e}}_{ir-1}}{dt} + l_r \tfrac{d\hat{\mathbf{e}}_{ir}}{dt}). \end{aligned} \quad (4)$$

The three cases not considered in (4) are as follows. When $i = 1$ and $j \geq 1$, the first term in (4) is not present. For the case when $i = 1$ and $j = 0$, $\mathbf{v}_{Cij} = \mathbf{0}$. Finally, for the case when $i \geq 1$ and $j = 0$, $\mathbf{v}_{Cij} = \mathbf{v}_{Ci-1\ 4}$.

The rotational kinetic co-energy contained in unit i is

$$T^*_{rot,i} = 2I_{i1}\dot{\phi}_i \quad (5)$$

where I_{i1} is the centroidal mass moment of inertia of link 1 and 3. Given that $m_{i4} = m_{i0}$, the total kinetic co-energy of the system can be written

$$\begin{aligned}T^* &= \sum_{i=1}^{N_2}\Big(\sum\nolimits_{j=0}^{4}(m_{ij}\mathbf{v}_{Cij}\cdot\mathbf{v}_{Cij}) \\ &\quad -\tfrac{1}{2}m_{i4}(\mathbf{v}_{Ci0}\cdot\mathbf{v}_{Ci0}+\mathbf{v}_{Ci4}\cdot\mathbf{v}_{Ci4}) \\ &\quad +2I_{i1}\dot{\phi}_i^2 + \tfrac{1}{2}m_{pi}(\dot{y}_{pi}^2+\mathbf{v}_{Ci2}\cdot\hat{\mathbf{j}})^2\Big). \end{aligned} \quad (6)$$

The total potential energy contained in the compliant elements is given by

$$\begin{aligned}V &= \sum_{i=1}^{N_2}\big(2(k_a+k_c)\phi_i^2 \\ &\quad +k_x l_1^2\left(\cos(\theta_0+\phi_i)-\cos(\theta_0)\right)+k_y y_{pi}^2\big). \end{aligned} \quad (7)$$

The generalized force acting on the y_{pi} coordinate is identically zero. The generalized force $\Xi_{\phi i}$ acting on the coordinate ϕ_i is

$$\Xi_{\phi i} = -f_{0i}l_1\sin(\theta_0+\phi_i). \quad (8)$$

Therefore, defining $\{\xi\} = [\phi_1 \quad y_{p1}..., \phi_{N2} \quad y_{pN2}]^T$ and $\{\Xi\} = [\Xi_{\phi 1} \quad 0..., \Xi_{\phi N2} \quad 0]^T$, the equations of motion are given by Lagrange's equations in standard form:

$$\frac{d}{dt}\left(\frac{\partial\mathcal{L}}{\partial\{\dot{\xi}\}}\right) - \frac{\partial\mathcal{L}}{\partial\{\xi\}} = \{\Xi\}^T \quad (9)$$

where $\mathcal{L} = T^* - V$ is the difference of (6) and (7). The equations of motion are considered explicitly for the case of a single second layer unit in the following sub-section.

C. Dynamics of a Single Second Layer Unit

The physical actuator prototype shown in Fig. 5 consists of a single second layer unit, which is a limiting case of the dynamics discussed in the previous section. The expected motions of the rhombus links are approximately 5 degrees. Therefore, using the standard linear approximations to $\sin(\theta_0+\phi_i)$ and $\cos(\theta_0+\phi_i)$ about $\phi = 0$, the application of (9) yields the following linear system:

$$\begin{bmatrix} m_{11} & m_{12} \\ m_{12} & m_{22}\end{bmatrix}\begin{Bmatrix}\ddot{\phi}_1 \\ \ddot{y}_{p1}\end{Bmatrix} + \begin{bmatrix} k_{11} & 0 \\ 0 & k_{22}\end{bmatrix}\begin{Bmatrix}\phi_1 \\ y_{p1}\end{Bmatrix} = \begin{Bmatrix}\frac{1}{2}\Xi_{\phi 1} \\ 0\end{Bmatrix}. \quad (10)$$

where

$$\begin{aligned}m_{11} = & l_1^2\left[\tfrac{1}{4}m_1 + m_2 + m_3\left(\tfrac{5}{4}+\cos 2\theta_0\right)\right. \\ & +m_4(1+\cos 2\theta_0) + m_p\left(\tfrac{1}{4}+\tfrac{1}{4}\cos 2\theta_0\right)\big] \\ & +2I_1, \end{aligned} \quad (11)$$

$$m_{12} = \tfrac{1}{2}m_p l_1\cos\theta_0, \quad (12)$$

$$m_{22} = \tfrac{1}{2}m_p, \quad (13)$$

$$k_{11} = 2(k_a+k_c) + k_x l_1\sin^2\theta_0, \quad (14)$$

and

$$k_{22} = k_y. \quad (15)$$

IV. IMPLEMENTATION AND EXPERIMENT

A. Prototype Construction

A prototype was constructed for experimental investigation. The prototype is shown in Fig. 5 and consists of six first-layer units contained within a bronze outer rhombus, i.e. the second layer strain amplification. All interunit and interlayer connections were made using conventional epoxy.

This prototype design uses a commercially available TF-PZT stack actuator produced by Cedrat, Inc. [27]. This PZT stack has an approximate blocking force of 460 N, a free displacement of 12 μm, and a maximum continuous voltage of 150V. Along the output axis of the amplification mechanism, this first layer unit produces a free displacement of 80 μm. Thus, when placed in series, the 6 first-layer units have a free displacement of 480 μm. The second layer amplifier, i.e. the outer rhombus, was designed to achieve free displacement of 3.08 mm with the body length along the output axis was kept to only 13 mm, yielding a total strain of 23.7%. The measured value of the second layer free displacement output was 2.49 mm, giving an effective strain of approximately 20%.

B. Experimental Validation

A frequency response test was performed as a validation of the linear dynamic equations in (10). The transfer function between the link 4 displacement Δr_4 and the input force $f_0(t)$, denoted by $\Delta R_4(s)/F_0(s)$, was identified. The displacement Δr_4 represents the unrestrained ouptut of the

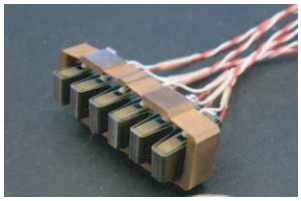

Fig. 5. Physical prototype consisting of 6 serially connected first layer units (Cedrat, Inc.) contained within an outer rhombus

rhombus mechanism and was therefore chosen as the variable for dynamic displacement measurements.

The test apparatus shown in Fig. 6 was used to measure the response of the prototype mechanism. The overall construction provides a single rigid constraint that aligns the actuator output axis with the measuring axis of a Micro-Epsilon ILD 1401-10 laser displacement sensor. All data were acquired using a PCI-6036E data acquisition card and LabVIEW^{TM} 7.1. Voltages were applied to the PZT stacks using a Cedrat CA-45 amplifier.

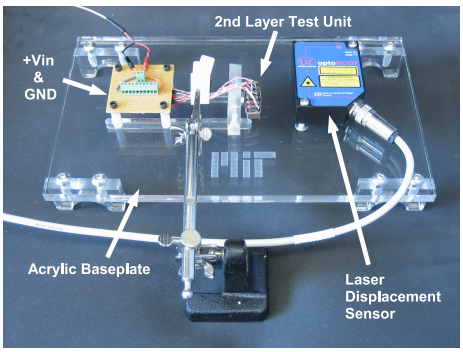

Fig. 6. Test equipment designed for measurement of actuator dynamic performance

For the transfer function identification experiment, a chirp voltage input V_{in} was applied in parallel to the six PZT stacks in the first layer. To assure adequate signal power within the actuator bandwidth, the chirp frequency ranged from 0.3 Hz to 500 Hz, with a peak amplitude value of 50 V and a minimum value of 0 V. The input voltage and output displacement were measured using the aforementioned equipment. The input force f_0 in the model is approximated by assuming a rhombus input stiffness of 0.04 $N/\mu m$ and calculating the maximum force applied by the first layer. This calculation yields 3.08 N for an input voltage of 50V. The force is then taken to vary sinusoidally from 0 to this value; therefore $f_0 \approx 0.062 V_{in}$.

The theoretical transfer function $\Delta R_4(s)/F_0(s)$ was computed using (10), and the parameters in Table I. Note that a multiplicative DC gain factor of $2l_1 \cos\theta_0$ was inserted in the theoretical transfer function to account for the kinematic tranformation between joint space coordinate ϕ and the output displacement $\Delta r_4(t)$. In Table I, the lumped horizontal stiffness and vertical stiffness parameters k_x and k_y were set based on a weighted least squares between the model and measured system, with weighting 0.5 decades above and below each resonant peak. The response of the measured system and the theoretical system are plotted together in Fig. 7.

TABLE I

PARAMETERS USED IN THEORETICAL MODEL

Parameter	Symbol	Value	Units
Link 1 and 3 Mass	m_1	0.345	g
Link 2 Mass	m_2	0.692	g
Link 4 Mass	m_4	0.0851	g
First Layer Mass	m_p	12	g
Length of Oblique Links	l_1	12.9	mm
Flexure Zone Length	L_f	3.51	mm
Flexure Thickness	t_f	0.1	mm
Rhombus Width	b	5.01	mm
Lumped Horizontal Stiffness	k_x	12	N/mm
Lumped Vertical Stifness	k_y	4.3	N/mm
Link 1 and 3 Inertia	I_1	4.3	kg $\cdot m^2$
Elastic Modulus	E	110	GPa
Initial Link Angle	θ_0	8	deg

The theoretical mode shapes and natural frequencies are readily obtained by solving the standard matrix eigenvalue problem. The fundamental mode exhibits in phase motion of the piezo unit and the rhombus vertical vibration. The second mode exhibits opposing phase motion of the piezo units of the rhombus. The measured frequencies for these modes were 61.1 Hz and 303 Hz respectively. The corresponding theoretical values were 49.3 Hz and 219 Hz. The complex zero frequency of the model resides at 134.7 Hz with the measured value residing at 84.1 Hz.

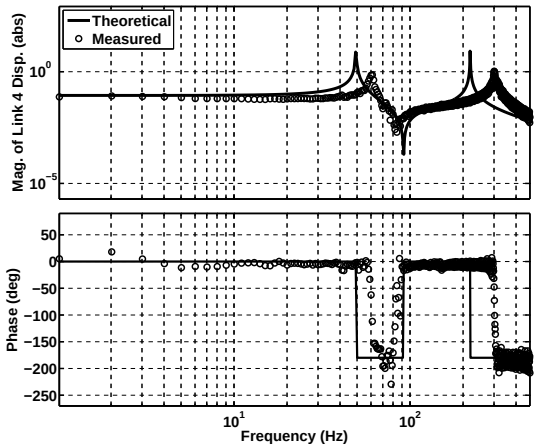

Fig. 7. Theoretical and measured frequency response of a second layer unit

C. Model Competence

There is close agreement between the measured system behavior and the theoretical response of the linearized system. This indicates that the linear model assumption is valid and the model is competent to describe the dynamics of a second layer unit in the frequency range of interest. Furthermore, the

data indicate that the assumed system order and pole-zero topologies are fundamentally correct.

A disparity between the measured and modeled responses arises due to lack of damping in the model. The unmodeled dynamics of the wiring would tend to act as increased stiffness, serving to raise the natural frequencies in the real system over the theoretical case. Also, recall that the axial stiffness and mass of the flexures was been neglected and the torsional spring approximation introduces some error for the large value of L_f. The complex zero frequency in the frequency domain models resides at $w_z^2 = \sqrt{k_{22}/m_{22}}$, whereas the measured frequency was considerably lower in both experiments. The likely cause of this difference is the uncertainty in the lumped vertical stiffness k_y and the piezo mass m_p.

The foregoing validation of the actuator model provides a firm basis for application and control of the actuator, which is disccused in the following section.

V. FLAPPING SYSTEM DYNAMICS

Several successful flapping aerial robots have been constructed and some ornithopters are commercially available. These robots form an important subclass of robotic aerial vehicles. Several military and commercial applications have been identified such as reconaissance and operation in hazardous environments. A successful flapping robot requires a design that minimizes weight and produces the appropriate aerodynamic forces. Such design issues are beyond the scope of the test system described here, but complete discussions can be found in [7], [23], [24], [25].

The second layer actuator unit was coupled to a flapping system as shown in Fig. 8.

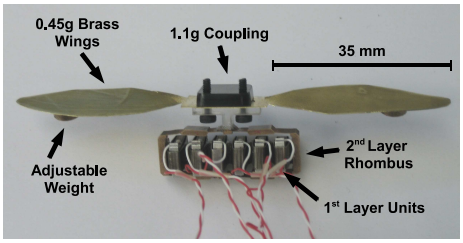

Fig. 8. Flapping system used to illustrate the resonance and servo capabilities of the actuator

The system introduces additional vibratory modes that may be modeled as shown in Fig. 9. This model considers only the a single dominant vibration mode based on the moving mass of the wings coupled elastically to link 4 of the second layer prototype. A w subscript is given to each lumped quantity relating to the wing load.

A. Extension of the Dynamic Model

For simplicity, the damping b_w shown in Fig. 9 will be neglected. Also, although it is utilized in most flapping flight robots, the torsional oscillation mode of wings is not included in the model. Therefore, the dynamics of the wing loading

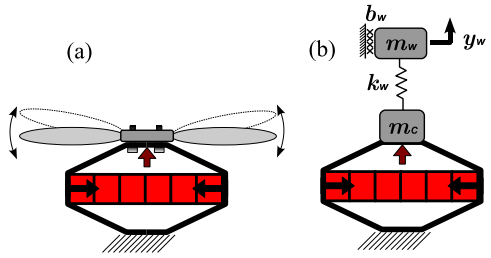

Fig. 9. (a) Flapping system (b) Model showing the lumped approximation of the dominant wing behavior

may be introduced into the theoretical model of III-C as follows.

First the coupling mass m_c must be added to link 4: $m_4' = m_4 + m_c$. The oscillating wing mass also contributes an additional term to the m_{11} parameter in (11) to yield m_{11}':

$$\begin{aligned} m_{11}' &= l_1^2 \left[\tfrac{1}{4}m_1 + m_2 + m_3\left(\tfrac{5}{4} + \cos 2\theta_0\right)\right. \\ &\quad \left. + m_4'(1 + \cos 2\theta_0) + m_p\left(\tfrac{1}{4} + \tfrac{1}{4}\cos 2\theta_0\right)\right] \\ &\quad + 2I_1 + m_w l_1^2(1 + \cos(2\theta_0)). \end{aligned} \tag{16}$$

The wing mass motion is inertially coupled to the motion in the other coordinates through m_{13} where $m_{13} = m_w l_1 \cos\theta_0$. The diagonal mass term for the y_w coordinate is $m_{33} = \frac{1}{2}m_w$. Finally, the stiffness parameter $k_{33} = k_w$ is introduced to model the elastic potential energy stored in the wing. All other design parameters and generalized forces remain as previously defined. Therefore, the extended dynamic equations may be expressed as a 3×3, 6th-order, inertially-coupled system.

B. Resonance Tuning

Flapping flight involves transient periods of high frequency wing movement, such as in takeoff and landing, as well as steady state flapping dynamics at an intermediate frequency. To achieve maximum efficiency, the system should be capable of resonating at various frequencies. This idea is also dicussed in [7] for a hypothetical pigeon sized bird and in [23] for microaerial vehicles.

The design space for tuning resonance parameters encompasses both the cellular actuator and the load. One possibility is to design the oscillatory modes of the system to coincide with the different flapping regimes and then drive the system to different resonant peaks using closed loop frequency control techniques such as a phase locked loop. Another possiblity is to change the configuration or distribution of mass in the system, which may be accomplished using another cellular actuator.

As an example of configuration change, experiments were performed using a double and half scheme for the wing mass. The alterations of the wing load achieved significant shifts in the fundamental flapping frequency. The nominal value for the wing mass was m_w = 0.45 g. The measurement displacement were taken at the wing coupling using the

measurement system described for the unloaded second layer unit. The results of the experiment are shown in Fig. 10.

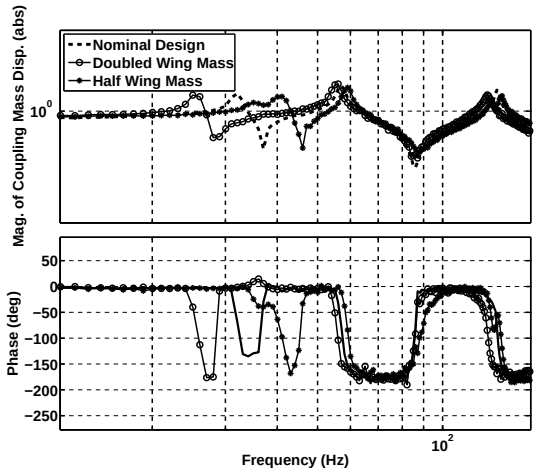

Fig. 10. Measured frequency response of the flapping system coupling mass

The lowest frequency mode shifts from 25 Hz to 41 Hz with the change in mass. The nominal first mode frequency is 32 Hz. These wingbeat frequencies are in a reaonable range for dragonfly sized robots to achieve sufficient lift for flight [23]. Notice that the higher frequency modes are relatively unaffected by the change. The effects the change in the wing mass properties are accurately predicted by the theoretical model discussed in the previous section. The theoretical results are shown in Fig. 11 for k_w = 11 N/m; m_c = 1.1 g; and m_w = 0.45 g, 0.9 g, and 0.22g.

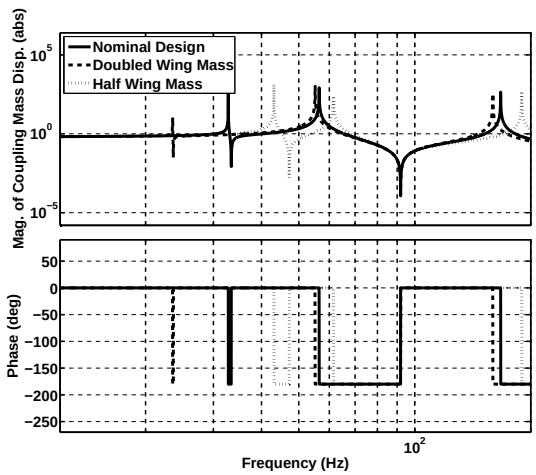

Fig. 11. Theoretical frequency response of the flapping system coupling mass

The model predicts that the lowest frequency mode shifts from 23.5 Hz to 43.1 Hz with the nominal value at 32.8 Hz. Therefore, the model of the wing dynamics can accurately predict the behavior of the resonances when the system is subject to parameter changes. This aspect of the dynamic model is crucial when the system must operate in a stable servo control mode as discussed in the following section.

C. Servo Control of Wing Position

For gliding maneuvers, an aerial robot must be able to quickly servo the wings between various positions. During flight, high speed force control may also be required [24]. Assuming a sensor such as a strain gauge bridge is mounted at the base of the wings to providing state information about the wing position, the control problem is still non-collocated. For this control system, fast servoing still may be achieved because the actuator has a very rapid open loop speed of response.

The position of the structural resonances appear to be well modeled and time invariant. Therefore, phase stabilization control is a viable alternative. However, given that flapping systems can operate in highly uncertain environments that change the system parameters, a more conservative gain stabilization controller is considered for the wing position.

The loop shape for the transfer function $Y_p(s)/F_0(s)$ is readily determined from the model of V-A. Based on achieving a unity gain crossover frequency with a gain margin of 14 dB and phase margin of 45°, the following cascade compensation is proposed:

$$G_c(s) = G_{lf}(s)G_{hf}(s) \tag{17}$$

where $G_{lf}(s)$ is the low frequency compensator transfer function

$$G_{lf}(s) = \frac{30s+1}{s^4} \tag{18}$$

reasonablent and $G_{hf}(s)$ is the high frequency compensator transfer function

$$G_{hf}(s) = \frac{1\times 10^9}{(0.006s+1)^3}. \tag{19}$$

The step response of wing position in closed loop is shown in Fig. 12. The rise time is approximately 70 ms and the settling time is approximately 150 ms. These results show that despite lightly damped resonances and non-collocated sensing, the actuator system can still achieve rapid speed of response for servo applications.

D. Design Implications

For the two-layer system considered, the resonant frequencies are readily tunable based on the inertial and compliant properties of the second layer rhombus and the load. For example, the thickness of the flexures has a cubic effect on joint stiffness. The inertial properties of the links can also be changed with the thickness of width parameters without large effects on the rhombus stiffness. Mass distribution changes were shown as an effective means for resonance tuning. To tailor the design for servo applications, joint damping may be added to the second layer by coating the leaf flexures with high loss polymeric materials. Furthermore, under known load conditions, phase stabilization notch filters could be employed based on the accurate plant model for the second layer units.

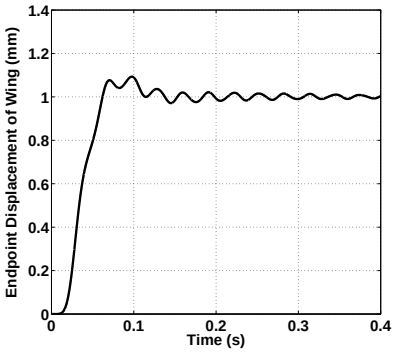

Fig. 12. Step response of wing position servo using a loop shaping controller

VI. CONCLUSION

This work describes the dynamics of a flexure-based cellular actuator design. The most unique dynamical feature of the proposed actuator design is its ability to mechanically resonate at several frequencies. For N_2 units there are $2N_2$ lightly damped natural frequencies. Maximum power transfer may be achieved by driving the system to one of the resonant peaks or by changing the location of the resonant peaks via configuration changes.

Overall, this work offers several contributions. First, a general cellular PZT design concept has been presented and a second layer unit prototype was constructed. A dynamic model suitable for control was formulated and analyzed in the frequency domain. The linearized dynamic model showed close agreement with experimental frequency response data. A flapping flight system was constructed to illustrate one possible application of the actuator. Resonance tuning and servo control were explored for the flapping flight test system.

Future work will focus on further prototype development and experimentation. Specifically, composite structures and serial connections of second layer units are being considered. Also, antagonistic arrangements of actuators are being explored as a means for stiffness control. Actuator position control may eventually be achieved using a broadcast feedback scheme described in [26]. Overall, the successful modeling discussed here shows that the cellular PZT actuator may be readily scaled, tuned, and controlled in myriad mobile robotic systems.

REFERENCES

[1] M.H. Dickinson , C.T. Farley , R.J. Full , M.A.R Koehl , R. Kram , and S. Lehman, "How Animals Move", *Science*, Vol. 288, pp. 100-106, 2000.

[2] H. Hanafusa and H. Asada, "A Robotic Hand with Elastic Fingers and Its Application to Assembly Processes", *Proc of FAC Symp. on Information Control Problems in Production Engineering*, pp. 127-138, October 1977.

[3] M. Raibert, "Legged Robots That Balance", MIT Press, April, 2000.

[4] R. Ghigliazza, R. Altendorfer, P. Holmes, and D.E. Koditschek, "Passively Stable Conservative Locomotion", *SIAM J. on App. Dynamical Systems*, Vol. 2, No. 2,pp. 187-218, 2003.

[5] J.G. Cham, S.A. Bailey, J.E. Clark, R.J. Full, and M.R. Cutkosky, "Fast and Robust Hexapedal Robots via Shape Depostition Manufacturing", *Int. J. of Robotics Research*, Vol. 21, Issue 10, 2002.

[6] J. Yan, M. Dickinson, J. Birch, M. Sitti, T. Su, and R. Fearing, "Wing Transmission for a Micro-Mechanical Flying Insect", *J. of Mircomechatronics*, Vol. 1, No. 3, pp. 221-237, 2002.

[7] K.K. Issac and S.K. Agrawal, "An Investigation Into the Use of Springs and Wing Motions to Minimize the Power Expended by a Pigeon-Sized Mechanical Bird for Steady Flight", *J. Mech. Design*, Vol. 129, pp. 381-389, 2007.

[8] D.L. Alshuler, R. Dudley, and C.P. Ellington, "Aerodynamics Forces of Revolving Hummingbird Wings and Wing Models", *J. Zoology*, London, Vol. 264, pp. 327-332, 2004.

[9] S. Frazier et. al., "Elasticity and Movements ofKohlCockroach Tarsus in Walking", *J. Comp. Physiology A*, Vol. 185, No. 2, pp. 157-172.

[10] K. Daltorio, A. Horchler, S. Gorb, R. Ritzmann, and R. Quinn, "A Small Wall-Walking Robot with Compliant, Adhesive Feet, *Proc. of IEEE/RSJ Int. Conf. on Robots and Systems*, Edmonton, Canada, 2005.

[11] J. Toomey and J. Eldredge Numerical and Experimental Investigation of the Role of Flexibility in Flapping Wing Flight, *AIAA Fluid Dynamics Conference and Exhibit*, pp. 2006-3211, 2006.

[12] K. Miyata and H. Hanafusa,"Modeling and Control of Pneumatic Rubber Actuator Drive Mechanism", *Proc. the 20th ISIR*, pp.677-684, 1989.

[13] S. Thongchai, M. Goldfarb, N Sarkar, and K. Kawamura, "A Frequency Modeling Method of Rubbertuators for Control Application in an IMA Framework", *Proc.of the American Control Conference*, Arlington, Virginia, 2001.

[14] J. Madden, P. Madden, P. Anquetil, and I. Hunter, "Load and Time Dependence of Displacement in a Conducting Polymer Actuator, *Materials Research Society Symposium - Proceedings*, Vol. 698, pp. 137-144, 2002.

[15] D. McCombie, T. Secord, and H. Asada,"Modeling and Observer Design for Polypyrrole Conducting Polymer Actuator Control Systems", *Proc. of the First IEEE/RAS-EMBS Int. Conf. on Biomedical Robotics and Biomechatronics*, pp. 432-436, 2006.

[16] J. Plante and S. Dubowsky, "On the Performance Mechanisms of Dielectric Elastomer Actuators", *Sensors and Actuators, A: Physical*, Vol. 137, No. 1, pp. 96-109, 2007.

[17] K. Otsuka and C. Wayman, *Shape Memory Materials*, Cambridge University Press, 1999.

[18] J. Ueda, T. Secord, and H. Asada, "Design of PZT Cellular Actuators with Power-law Strain Amplification", Accepted for Publication in *Proc. of IEEE/RSJ Int. Conf. on Robots and Systems*, San Diego, CA, 2007.

[19] V.K. Varma and W.E. Dixon, "Design of a Piezoelectric Meso-scale Mobile Robot: A Compliant Amplification Approach", *Proc. of IEEE Int. Conf. on Robotics and Automation*, Washington, D.C., pp. 1137-1142, 2002.

[20] N.J. Conway, Z.J. Traina, and S.G. Kim, "A strain amplifying piezoelectric MEMS actuator", *J. Micromechanics and Micromachining*, Vol. 17, pp. 781-787, 2007.

[21] H. Zhou, B. Henson, "Analysis of a diamond shaped mechanical amplifier for a piezo actuator", *Int. J. Adv. Manuf. Technol.*, Vol. 32, pp. 1-7, 2007.

[22] P. Jänker, M. Christmann, F. Hermle, T. Lorkowski, and S. Storm, "Mechatronics Using Piezoelectric Actuators", *J. of the European Ceramic Society*, Vol. 19, pp. 1127-1131, 1999.

[23] A. Cox, E. Garcia, and M. Goldfarb, "Actuator Development for a Flapping Microrobotic Mircoaerial Vehicle", *Proc. of SPIE Conf. on Microrobotics and Micromanipulation*, Vol. 3519, pp. 102-108, 1998.

[24] J. Yan, R.J. Wood, S. Avandhanula, M. Sitti, and R.S. Fearing, "Towards Flapping Wing Control for a Micromechanical Flying Insect", *Proc. of IEEE Int. Conf. on Robotics and Automation*, Seoul, Korea, pp. 3901-3908, 2001.

[25] N. Vandenberghe, S. Childress, and J. Zhang, "On Unidirectional Flight of a Free Flapping Wing," *Physics of Fluids*, Vol. 18, pp. 014102-014102-8, 2006.

[26] J. Ueda, L. Odhner, and H. Asada, "A Broadcast Probability Approach to the Control of Vast DOF Cellular Actuators", *Proc. of IEEE Int. Conf. on Robotics and Automation*, Orlando, Florida, pp. 1456-1461, 2006.

[27] CEDRAT Inc., http://www.cedrat.com/.

Preprint submitted to 2008 IEEE International Conference on Robotics and Automation. Received September 14, 2007.